# Silicon Nanopillars for Field-Enhanced Surface Spectroscopy

**Sabrina M. Wells,[†] Igor A. Merkulov,[‡] Ivan I. Kravchenko,[‡] Nickolay V. Lavrik,[‡,*] and Michael J. Sepaniak[†,*]**

[†]University of Tennessee, Knoxville, Tennessee 37996-1600, United States and [‡]Center for Nanophase Materials Sciences, Oak Ridge National Laboratory, Oak Ridge, Tennessee 37831-6487, United States

**ABSTRACT** Silicon nanowire and nanopillar structures have drawn increased attention in recent years due in part to their unique optical properties. Herein, electron beam lithography combined with reactive-ion etching is used to reproducibly create individual silicon nanopillars of various sizes, shapes, and heights. Finite difference time domain analysis predicts local field intensity enhancements in the vicinity of appropriately sized and coaxially illuminated silicon nanopillars of approximately 2 orders of magnitude. While this level of enhancement is modest when compared to plasmonic systems, the unique advantage of the silicon nanopillar resonators is that they enhance optical fields in substantially larger volumes. By analyzing experimentally measured strength of the silicon Raman phonon line (500 $cm^{-1}$), it was determined that nanopillars produced local field enhancements that are consistent with these predictions. Additionally, we demonstrate that a thin layer of Zn phthalocyanine on the nanopillar surface with a total amount of <30 attomoles produced prominent Raman spectra, yielding enhancement factors (EFs) better than 2 orders of magnitude. Finally, silicon nanopillars of cylindrical and elliptical shapes were labeled with different fluorophors and evaluated for their surface-enhanced fluorescence (SEF) capability. The EFs derived from analysis of the acquired fluorescence microscopy images indicate that silicon nanopillar structures can provide enhancements comparable or even stronger than those typically achieved using plasmonic SEF structures without the limitations of the metal-based substrates, such as fluorescence quenching and an insufficiently large probe volume. It is anticipated that dense arrays of silicon nanopillars will enable SEF assays with extremely high sensitivity, while a broader impact of the reported phenomena is anticipated in photovoltaics, subwavelength light focusing, and fundamental nanophotonics.

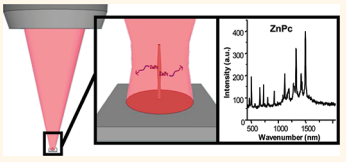


**KEYWORDS:** silicon nanopillars · axial illumination · fundamental $HE_{11}$ mode · large local field enhancement · FDTD analysis · SERS · SEF

Semiconductor nanowire and nanopillar structures have been a subject of significantly increased attention in recent years, largely due to the renewed interest in their unique properties that can be utilized in photon detection and solar energy applications.[1−8] Although semiconductor nanostructures with characteristic sizes on the order of 100 nm are generally too large for quantum confinement effects to take place,[9−11] optical properties of such nanostructures tend to deviate substantially from those of bulk semiconductors.[3,5,12−16] Such optical phenomena beyond the quantum confinement regime can be explained by the fact that optical resonators with sizes (diameters) approximately an order of magnitude smaller than the wavelength of light in vacuum can be implemented in semiconductors. Indeed, several semiconductor materials, in particular, silicon, possess very high refractive indices (>3.5) combined with low extinction coefficients in a portion of the visible spectrum and in the near-infrared. These properties make them uniquely suitable for creating low loss optical resonators with characteristic sizes of approximately 100 nm.

The complex and nontrivial nature of optical resonances in semiconductor nanowires and nanopillars clearly follows from a number of very recent studies in this area.[3,5,13−16] In particular, a series of recent studies by Brongersma's group[3,5,14] demonstrated that leaky mode resonances in semiconductor nanowires provide a powerful and elegant means to engineer light absorption in optoelectronic devices[5,17] and tune the color of silicon nanostructures.[14] Muskens *et al.*[18] showed that strong Mie-type internal resonances in vertically aligned semiconductor nanowire arrays lead to record levels of light scattering that can be tuned over a wide spectral range. Furthermore, the guided mode properties of individual silicon nanopillars can give rise to a palette of surprisingly vivid colors readily visible in bright-field microscopy.[16] Although this recent study has unambiguously demonstrated that individual silicon nanopillars exhibit a certain type of resonance due to the fundamental $HE_{11}$ guided mode, a remaining open question is whether significant enhancements of local field can be associated with this phenomenon and utilized in analytical optical techniques in analogy to localized surface plasmon resonance. To our best knowledge, the possibility of strong field enhancement associated with

* Address correspondence to lavriknv@ornl.gov, msepaniak@utk.edu.

Received for review October 25, 2011 and accepted March 4, 2012.

**Published online March 04, 2012**
**10.1021/nn204110z**

the fundamental guided mode in vertical silicon nanopillars has not been evaluated. Indeed, the majority of studies in this field focused on higher modes that have cutoff and are expected to exhibit a leaky mode resonance.[5] In these studies, asymmetric optical arrangements were used. In particular,[5,19] they described conical and cylindrical Si nanowires probed by a focused laser beam under normal and oblique angles of incidence. Under those conditions, the fundamental $HE_{11}$ mode could not be efficiently excited and, therefore, was not evaluated in those studies. On the other hand, illumination of an individual silicon nanopillar by a coaxial beam makes excitation of the fundamental $HE_{11}$ mode very efficient.[16] Previous studies in which such a coaxial illumination was used, however, focused on enhanced light absorption or scattering without reporting the magnitudes of local field enhancements.[5,19] For instance, simulations of the transverse electric field in the vicinity of a coaxially illuminated nanopillar reported very recently by Seo *et al.*[16] indicated maximum values of unity regardless of the wavelength due to the normalization method utilized. Modeling of the optical near-field in the vicinity of coaxially illuminated dual diameter germanium nanopillars indicated some degree of enhancement[2] but was not quantifiable due to the lack of an appropriate normalization. Theoretical analysis of germanium nanowires placed horizontally on a substrate was conducted in another study[17] and indicated enhancements in optical near-field intensity, $(E_{max}/E_0)^2$, in such systems up to a factor of 10. Another recent study by Sturmberg *et al.*[20] points to a nontrivial task of optimizing silicon nanopillar arrays for enhanced optical absorption. While this study provided an excellent analysis of the factors that determine modal dispersion and the magnitude of enhanced absorption of such arrays, evaluation of the local field enhancement in the vicinity of silicon nanopillars was beyond its scope.

Herein, we point to conditions when enhancement of local field in the vicinity of an individual silicon nanopillar is maximized and demonstrate experimentally that such conditions associated with $HE_{11}$ mode provide a new pathway to spectroscopic analytical techniques, including surface-enhanced fluorescence (SEF) and Raman scattering (SERS), which do not involve plasmons.

Although studies of semiconductor nanowires and nanopillars often take advantage of "bottom-up" technological strategies, such as vapor–liquid–solid (VLS) growth,[21–23] a deterministic technological strategy based on lithographic patterning is better suited for creating sparsely spaced silicon nanopillars with more flexible control over their shapes and dimensions. Consistent with our goals and our previous positive experience with nano- and microfabrication,[24–26] we relied on electron beam lithography (EBL) and anisotropic reactive-ion etching (RIE) to create silicon nanopillars

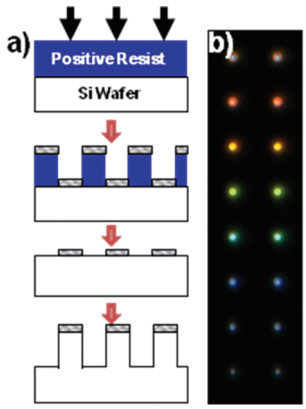


**Figure 1. (a) Fabrication sequence used for creating silicon nanopillars; (b) dark-field optical microscopy of type #2 nanopillars with average diameters ranging from 95 to 180 nm.**

analogous to the ones studied by Seo *et al.*,[16] however, with various shapes (Figure 1). Our rationale behind exploring nanopillars with distinct sidewall profiles was three-fold: (i) tapered shapes are known to improve coupling of $HE_{11}$ mode in cylindrical dielectric antennas;[27] (ii) nanopillars with variable cross sections exhibit resonances in a wider or multiple spectral regions;[2] and (iii) while anisotropic RIE of silicon offers good control over sidewall profile, it rarely yields perfectly vertical sidewalls. Previous work in our group focused on using EBL and RIE to create silicon nanopillar structures, metalized for plasmonic effects, to perform SERS with high sensitivity.[24] Relatively short pillars were found to maximize plasmonic and optical cavity contributions to the observed overall fields[26] and exhibited Raman enhancement factors (EFs) of $>10^9$ with high reproducibility. Here, we utilize similar technological approaches and demonstrate the potential of relatively long, narrow silicon nanopillars for achieving substantial nonplasmonic field enhancements. The spatial distributions and heterogeneity of the near-field intensity around the pillars are modeled using the finite difference time domain (FDTD) method. In analogy to theoretical evaluations of plasmonic nanostructures, we evaluate maxima in local field intensity, which are the highest values of the electric component of near-field intensity, $E_{max}^2$, normalized by the field intensity of the incident beam, $E_0^2$. The calculated field enhancements, $E_{max}/E_0$, in turn, allow one to estimate Raman EF based on the $(E_{max}/E_0)^4$ formula. This formula is known to give a fair approximation of the actual Raman EF in the case of small individual plasmonic particles.[28] For more complex geometries and for larger (micrometer size) particles, enhancement of the Raman dipole emission tends to be significantly reduced compared to the local field enhancement $E_{max}/E_0$.[28,29] Although the latter behavior may well be the case for several micrometer long silicon nanopillars, here we use the $(E_{max}/E_0)^4$ formula to estimate an upper theoretical limit of the Raman EF.

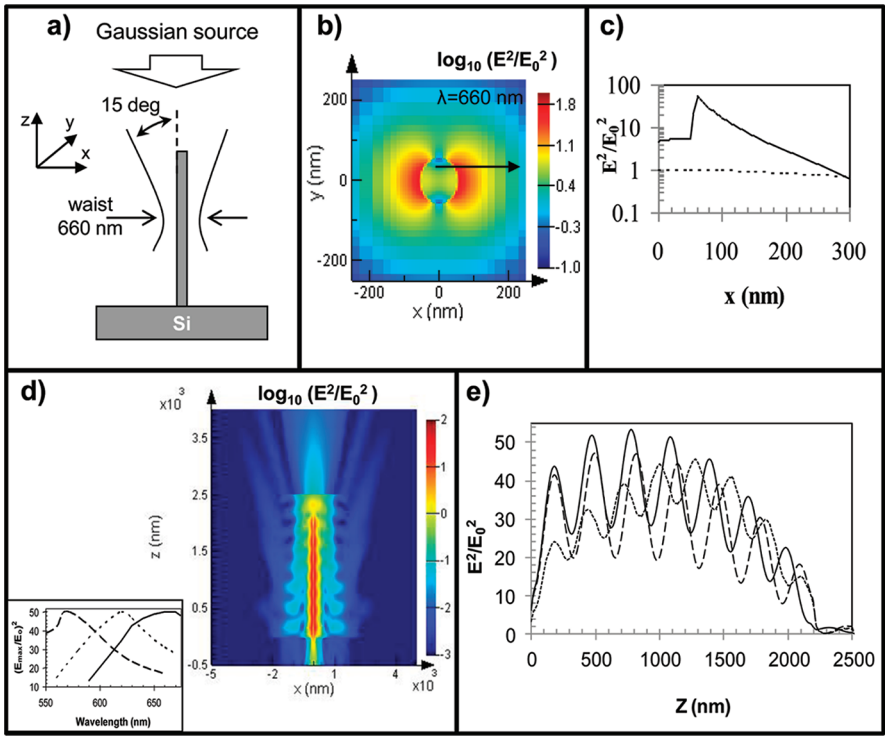


**Figure 2. FDTD simulations of a vertical Si nanopillar on a silicon substrate coaxially illuminated by a Gaussian beam: (a) schematic representation of the *X*−*Z* intersection of the 3D FDTD model used in this study; (b) normalized field intensity in the *X*−*Y* plane at *Z* = 800 nm; (c) normalized field intensity along the *X*-axis at *Y* = 800 nm in the region shown by the arrow in panel b in the vicinity of the pillar (solid curve) and without the pillar (dotted curve); (d) normalized field intensity in the *X*−*Z* plane intersecting the pillar axis; (e) normalized field intensity along the *Z*-axis in the vicinity of the pillar at *X* = 60 nm and *Y* = 0 nm calculated for 645 nm (dotted curve), 660 nm (solid curve), and 675 nm (dashed curve). All simulation data shown here except the inset in panel d are obtained for pillar height and diameter of, respectively, 2200 and 110 nm. Local field distributions in panels b−d are calculated for a wavelength of 660 nm and displayed on a logarithmic scale. The inset in panel d shows maximum intensity enhancements as a function of wavelength for 2200 nm long pillars with diameters of 90 nm (dashed curve), 100 nm (dotted curve), and 110 nm (solid curve).**

In order to demonstrate the analytical consequences of the enhanced near-fields in vicinity of a silicon nanopillar, we evaluate the raw spectroscopic signals (Raman or fluorescence) generated by the nanopillar itself or test analytes in close proximity and analyze the raw signal increases (RSI) corrected for the background signals and analyte amounts. Since we measured spectroscopic signals of an ensemble of analyte molecules under the widely varying near-field intensities, $(E_{max}/E_0)^2$ around the nanostructure under study, our reported average EF values are conservative estimates that are substantially below the actual maximum EF achieved in our experiments.

## RESULTS AND DISCUSSION

To identify the boundaries of the nanopillar design space and to drive successive iterations of our fabrication sequence, we carried out numerical simulations of our experimental system using the FDTD method. Our FDTD model closely resembled our experimental system and included an individual silicon nanopillar, a silicon wafer substrate, and a Gaussian light source impinging on the pillar coaxially (Figure 2a; further details of the FDTD model are given in the Materials and Methods section). Our evaluation of the FDTD model indicates that a wavelength-dependent enhancement of the local field intensity on the surface and in the immediate vicinity of a sufficiently long silicon nanopillar can reach more than 2 orders of magnitude. Our FDTD simulations conducted for nanopillars of different diameters revealed that 110 nm is the pillar diameter that corresponds to the strongest field enhancement at approximately 650 nm. This finding correlates well with the reflectivity minimum at approximately 630 nm reported previously for arrays of silicon nanopillars with 110 nm diameter.[16] We also found that maximum enhancement of the local field intensity increases significantly when pillar heights increase and also when the angular convergence of the incident beam decreases.

We conducted more detailed FDTD analysis for a pillar height of 2200 nm and beam divergence of 15° (Figure 2). These values correspond, respectively, to the longest nanopillars that we could reproducibly fabricate and to the smallest convergence angle that we could achieve in our experiments when illuminating nanopillars through a high-magnification (100×) microscope objective. The wavelength-dependent changes in the distribution of the electric component of the local field intensity in the plane perpendicular to the

**TABLE 1. Ability of Silicon Nanopillars with Various Shapes and Heights To Enhance Intrinsic Raman Scattering[a]**



| Type | Height | Optimum Diameter | | Shape | Si line Ratio | $(E_{max}/E_0)^4$ |
|---|---|---|---|---|---|---|
| | | CAD | Average | | | |
| #1 | 400 nm | 120 nm | 120 nm | Slightly positive taper (91° sidewall) | 0.32 | 1020 |
| #2 | 825 nm | 130 nm | 105 nm | Negative taper (87° sidewall) | 0.65 | 1296 |
| #3 | 700 nm | 90 nm | 100 nm | Positive taper at top (93°); cylindrical bottom | 1.47 | 1760 |
| #4 | 800 nm | 120 nm | Not available | Positive taper at top (93°); cylindrical bottom | 3.91 | 1600 |
| #5 | 975 nm | 80 nm | 95 nm | Positive taper at top (93°); cylindrical bottom | 7.04 | 1936 |
| #6 | 1300 nm | 115 nm | 165 nm | Positive taper at top (93°); negative at bottom (88°) | 5.76 | 2200 |
| #7 | 2300 nm | 120 nm | 185 nm | Positive taper at top (93°); negative at bottom (88°) | 11.0 | 2704 |


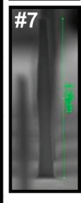


[a] In each series of nanopillars of the same type, the optimum diameters correspond to a nanopillar that exhibited strongest enhancement of the silicon Raman line. Note that Si line ratio is calculated as a raw signal enhancement; (pillar based signal − off-pillar background)/background. Values for $(E_{max}/E_0)^4$ based on the FDTD method appear for each type. Representative examples of several pillar types are shown as SEMs on the right.

nanopillar axis are indicative of the fundamental, $HE_{11}$, mode (Figure 2b) and consistent with the results reported previously.[16] Importantly, a strongly enhanced field concentrates in extremely small areas in the nanopillar vicinity. As can be seen in Figure 2c, normalized field intensity, $E^2/E_0^2$, decays from approximately 50 to 10 within less than 50 nm from the nanopillar surface. Evaluation of the local field intensity in the $Y-Z$ plane intersecting the nanopillar axis and parallel to the polarization plane (Figure 2d,e) provides additional insights into the magnitude and mechanisms of the observed enhancement. As expected, a periodic pattern superimposed over the local intensity distribution is formed due to standing waves at the reflecting surface of the silicon substrate (Figure 2d,e). The maximum field intensity is observed at $Z \approx 800$ nm, that is, shifted slightly along the $Z$-axis with respect to the beam waist (centered at $Z = 1000$ nm) toward the substrate. We analyzed the wavelength-dependent nature of this enhancement (see inset in Figure 2d) and used it for guidance in selecting nanopillar diameters for our experiments in various spectral regions. Consistent with the guidance obtained from our FDTD analysis, we fabricated a series of silicon structures with nanopillars of various heights and shapes and average diameters in the range of 95 to 165 nm. In order to evaluate the ability of such structures to enhance Raman scattering and fluorescence signals and to demonstrate their versatility in these potential applications, we devised and conducted three types of experiments that focused on (i) analysis of the enhanced Raman scattering in silicon, (ii) fluorescent microscopy of nanopillar structures labeled with NHS-rhodamine and fluorescein isothiocyanate (FITC), and (iii) Raman spectroscopy of a thin layer of zinc phthalocyanine (ZnPc) deposited onto the nanopillar and surrounding area. Results of these experiments provide the first experimental evidence that individual silicon nanopillars can be used as versatile and highly efficient enhancers of local field intensity with utility in analytical optical techniques.

**Nanopillar Fabrication.** A fabrication sequence similar to the ones reported in our own previous studies[24] and by other groups[15,16] was used to create silicon nanopillar structures. A more detailed description of the fabrication process can be found in the Materials and Methods section. An important feature of our structures that differentiates them from the majority of previously implemented silicon nanopillars was a large area surrounding each individual nanopillar devoid of additional features so as to allow for optical interrogation without interference from other structures (see Figure 1a). In addition to the guidance from our numerical modeling, feedback from the structural analysis of nanopillars fabricated in previous trials determined the parameters that would be used with subsequent fabrication. As a result, several pillar "types" were created (Table 1). As can be seen in the table, each pillar type had a distinctive height and shape. Each pillar type included a series of pillars that spanned a range of diameters, typically 75 to 160 nm. It should be noted that diameters of the structures can be described in two ways. The first description is according to the diameter of the circular CAD feature used to

pattern the Cr mask. It is important to emphasize that this diameter tends to deviate from the actual size of the fabricated nanopillar since the sidewall produced by the RIE is rarely perfectly vertical. The other way to describe pillar diameter is to calculate the average diameter of each nanopillar based on the analysis of its scanning electron microscope (SEM) images. While this parameter is more directly related to the actual pillar size, relying on structural metrology based on SEM imaging has its own disadvantages. In particular, the accuracy of SEM quantitative measurements is known to vary depending on the type of sample, accelerating voltage, *etc.* and typically is not better than 10%.

**Enhancement of Intrinsic Silicon Raman Scattering.** Once a variety of silicon nanopillar structures had been fabricated, a series of optical probing experiments were conducted. In our initial screening tests, we used dark-field optical microscopy, which could clearly visualize each individual nanopillar as a bright light-scattering spot, often characterized by a vivid color (Figure 1d). Defective and missing nanopillar structures could be readily identified in dark-field optical microscopy observations. Subsequently, Raman spectroscopy mapping of our samples was performed using a confocal Raman microscope with a 633 nm HeNe laser excitation. In these experiments, we mapped the intensity of the silicon line (phonon line of the single crystal silicon) at 500 $cm^{-1}$ over the 5 $\mu$m $\times$ 5 $\mu$m areas surrounding each nanopillar. As seen in Figure 3, the intensity map of the silicon line has a maximum that coincides with the nanopillar position. The amplified silicon Raman signal due to the presence of the pillar can also be clearly seen in the spectra shown in Figure 3 below the intensity map. Normalized increases in the silicon band areas for on-pillar (*signal*) *versus* off-pillar (*background*) laser spot positions are given in Table 1. These values determined as [(signal − background)/background] were used to judge the *relative* enhancement of the Raman scattering by various nanopillar types in analogy to the methodology described previously.[19] It should be emphasized, however, that our Raman spectroscopic measurements of silicon nanopillar structures on silicon substrates always included a significant background signal from the substrate.

Several notable trends can be seen in Table 1. The most readily recognizable trend is that taller nanopillars exhibited higher signal enhancement (*i.e.*, compare type #6 with type #7). However, an explanation of this trend based on the larger surface area of taller pillars can be completely ruled out since enhancements of the silicon Raman line also depended dramatically on the pillar shape. In particular, enhancements of Raman scattering by type #3 nanopillars with undercut (negatively sloped) sidewalls were generally significantly lower compared to the other nanopillar types characterized by tapered (conical) shapes. While a more extensive FDTD analysis of nanopillar models with various shapes could provide valuable insights in understanding this difference, it is reasonable to assume that the tapered region improves coupling of the scattered light into the collecting optics in analogy to the tapered regions of dielectric rod antennas.[27] The strongest enhancement of the silicon line Raman scattering was observed in the case of tallest pillars (type #7, shown in Table 1): the raw signal ratio was found to be 11. This value was used for calculations of the enhancement factor EF (see below).

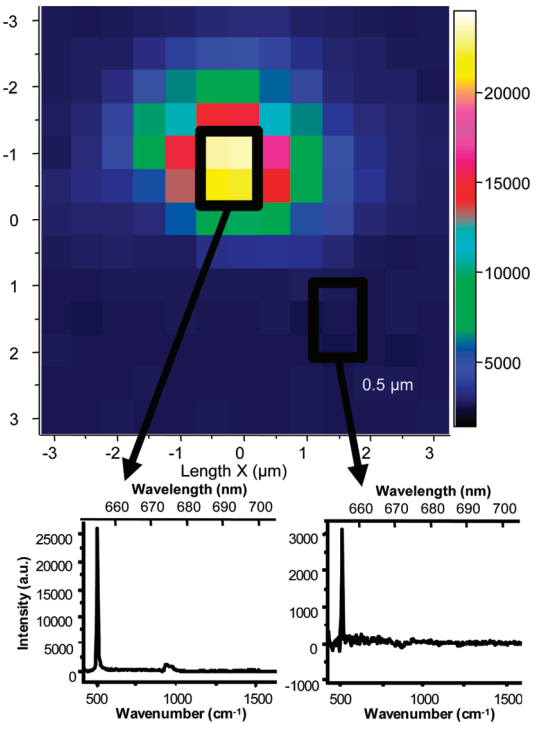


**Figure 3. Raman map (top) shows enhanced intensity of the silicon phonon line due to the presence of a type #4 silicon nanopillar with an average diameter of 95 nm. Also shown are complete Raman spectra measured on (bottom left) and off (bottom right) the nanopillar.**

Figure 4 shows analysis of the raw Raman signal enhancement for nanopillars with two different shapes (Figure 4a−c) with average pillar diameters in the range of 95−210 nm. The values in Figure 4 are the averages of measurements on three separate nanopillars of the given diameter, with the RSD for each average better than 10%. It is worthy to note that, in the case of a perfectly cylindrical nanopillar, FDTD analysis predicts a straightforward relationship between the pillar diameter and the wavelength at which the local field undergoes maximum enhancement. In particular, our FDTD simulations predict that the nanopillar diameter needs to be approximately 110 nm for the strongest local field enhancement to be achieved at 660 nm (see Figure 2e). Taking into account the Stokes shift of approximately 20 nm for the Raman silicon line in our measurements (*i.e.*, wavelengths of probing and scattered light are, respectively, 632 and 652 nm), this

prediction correlates well with the trend shown in Figure 4b for type #5 nanopillars. It appears, however, that optimum average diameters experimentally determined for other nanopillar shapes, such as type #6 with noticeably narrower top and wider bottom, may deviate from this prediction. This deviation is most likely a complicating consequence of the tapered nanopillar shapes with variable cross sections. On the other hand, type #5 and type #6 nanopillars fabricated using the same CAD dimensions had significantly different average diameters (Figure 4) due to the different etching protocols. An important practical implication of these observations is that a pattern with same CAD diameter can be used to create nanopillars with different average diameters optimized for different wavelengths.

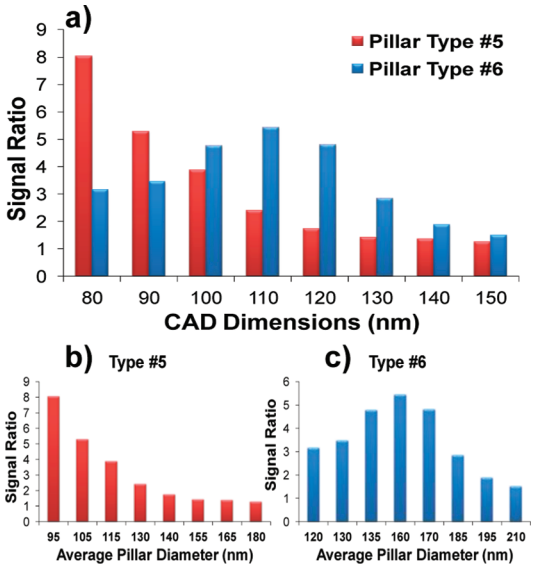


Figure 4. (a) Silicon Raman signal ratio (on *versus* off nanopillar, 500 $cm^{-1}$) trend of two different types and heights of nanopillars based on the CAD (Cr mask diameter at the top of the structure). (b) Trend with average pillar diameter of type #5 pillar (see Table 1). (c) Trend with average pillar diameter of type #6 pillar.

**Enhanced Fluorescence.** Strong enhancements of the Raman silicon line generated by type #5 and #7 nanopillars encouraged us to use them in subsequent fluorescent microscopy experiments and additional Raman scattering measurements. Our hypothesis was that local field enhancements in vicinity of silicon nanopillars should enable enhanced fluorescence measurements in analogy to enhanced fluorescence in the vicinity of plasmonic nanostructures and metal surfaces.[30−35] Such systems enabling enhanced fluorescence are of great interest in chemical and biological analysis.[36,37] They have recently become a subject of more extensive studies due to advances in nanotechnology and chip level fluidic systems.[38,39] A common feature of many previously implemented systems that exhibit enhanced fluorescence is the presence of a plasmonic metal feature. By contrast to these studies, here we demonstrate that practically significant enhanced fluorescence can be achieved in a metal-free system by taking advantage of strong local field enhancement in the vicinity of an appropriately designed silicon nanopillar.

Type #5 nanopillar structures were labeled with NHS-rhodamine dye using techniques described in the Materials and Methods section. The fluorescent image in Figure 5 shows a set of NHS-rhodamine-labeled nanopillars with average diameters ranging from 95 to 165 nm (left to right). Each column of nanopillars in Figure 5 corresponds to the same nominal size. Dramatically increased fluorescence intensity

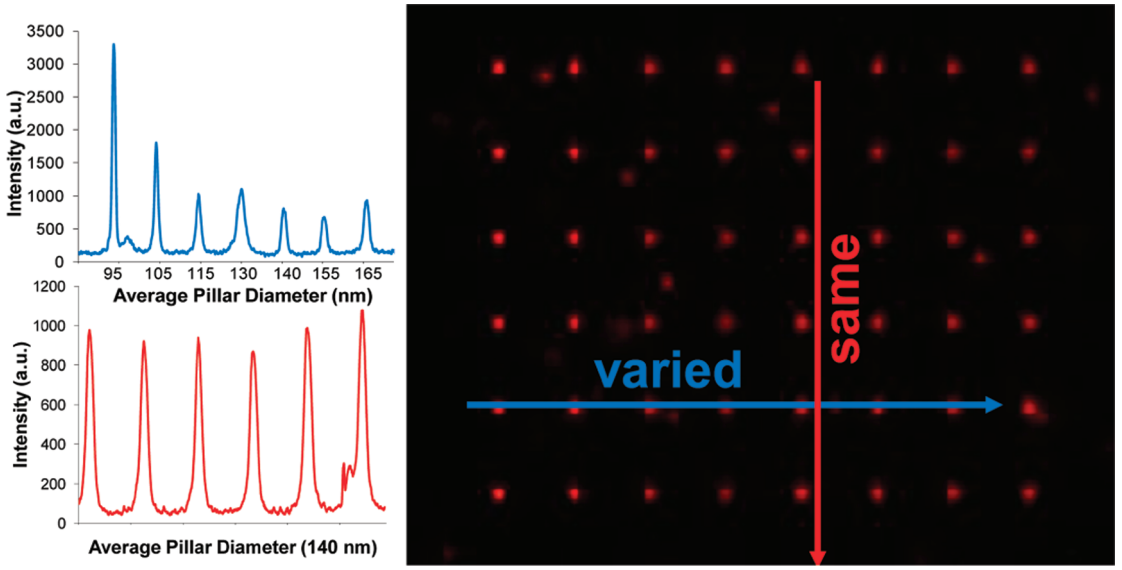


Figure 5. Fluorescence image of nanopillars ranging from 95 to 165 nm in average diameters and coated with NHS-rhodamine. The corresponding intensity plot (blue) correlates well with the trend seen in Figure 4. The intensity is also reproducible for a given average diameter (red).

in the regions corresponding to each nanopillar is clearly seen in Figure 5. The red fluorescence intensity maximizes in the region occupied by the smallest pillars with an average diameter of 95 nm. Note that an examination of a blank sample with no fluorescent dye was conducted and produced negligible signal (no pillar *vesus* nonpillar difference). The excitation band used to acquire these images is centered at approximately 540 nm. Notably, the 95 nm diameter correlates reasonably well with the results of our FDTD analysis that predicts local field enhancement to maximize at 580 nm for this nanopillar diameter. The fluorescence intensity profile measured across a series of nanopillars with the same targeted diameter of 140 nm indicates excellent reproducibility of the observed enhancement (a relative standard deviation of 7%). The type #5 nanopillar structures produced a raw fluorescence signal enhancement of approximately 35 for each individual pillar (see Figure 5). This value compares favorably with many previously demonstrated SEF systems, such as metal nanocomposites,[40] silver nanoparticles,[41,42] and thin metal films.[43,44] While these systems have been proposed for a variety of applications, including protein binding and immunoassays, the observed raw enhancement is generally 10−15 times in the best performing systems[45] with an exception of plasmonic nanostructures similar to SERS-active "hot spots". Strongest fluorescent enhancement, up to 2 orders of magnitude, has been achieved by placing a fluorescently labeled sample on a SERS-active substrate in vicinity of a hot spot.[31] However, transition from fluorescence enhancement to fluorescence quenching is common when a sample molecule is extremely close to the metal surface.[46] Furthemore, enhanced field in the vicinity of the silicon nanopillars (see Figure 2c) has a significantly larger total volume compared to the majority of plasmon-based SEF systems. Enhancement of fluorescence signals within larger analyte volume combined with the absence of fluorescence quenching means that there are fewer experimental constraints when analyte sequestering reagents are immobilized on the nanopillar. In particular, we envision a system in which analytes are not quenched due to contact with the nanopillar surface while large bioaffinity molecules such as capture antibodies are still within the reach of the high fields.

In order to further demonstrate the versatility of our approach and its potential for a variety of analytical fluorescence techniques, we prepared a series of nanopillar structures characterized by elliptical cross sections and labeled them with FITC. In order to fabricate this series of nanopillars, elliptical CAD patterns with two different dimensions and the major axis oriented at incrementally rotated angles were created (depiction at the top of Figure 6). These elliptical nanopillars were etched using the same RIE recipe as the one used to etch type #5 pillars. In addition to demonstrating SEF using another dye, the goal of these experiments was to take advantage of polarization-dependent resonances in elliptical dielectric resonators. Our hypothesis was that, in the case of polarized incident light, effective diameters of elliptical nanopillars will depend on the relative orientation of the polarization plane with respect to the ellipse's major axis. This hypothesis was indeed confirmed by our experimental observations. When illuminated by nonpolarized light, the fluorescence intensity of individual elliptical pillars was fairly uniform across the array with the incrementally rotated major axis. Under polarized light, however, fluorescence intensity depended noticeably on the major axis orientation. As can be seen in the intensity plots for b and c in Figure 6, the horizontal orientation (major axis coinciding with the polarization plane) gave a stronger signal compared to nanopillars with the major axis oriented at arbitrary angles or vertically. Note that both the polarized and nonpolarized light yield similar trends in the intensity plots for the circular pillars.

**Enhanced Raman of a Thin Sample Layer on Nanopillars.** The key strength of Raman spectroscopy is that it provides chemical information about analyzed samples. However, due to extremely small cross sections of inelastic scattering interactions, Raman spectroscopy is not a sensitive technique unless enhancement of the Raman signal is achieved *via* the use of appropriately designed surfaces. As such, SERS has become more popular for both chemical and bioanalysis due to the enhanced sensitivity.[38] While SERS is a well-established approach that takes advantage of the localized surface plasmon resonance in noble metal nanoparticles and on rough surfaces of noble metals,[47,48] recent theoretical study has indicated that plasmonless SERS may also be possible.[29] Indeed, one of the biggest continued challenges in SERS as an analytical technique has been scarcity and irreproducibility of hot spots largely due to polymorphism and surface reactivity of metal nanoparticles. Furthermore, when only a small number of sample molecules are available, then their precise delivery to a particular hot spot represents even a bigger challenge. Therefore, field concentration by silicon nanopillars may help to bridge the gap between micro-Raman spectroscopy, which relies on conventional refractive optics and is a viable analytical technique but lacks sensitivity for demanding applications, and SERS, which offers excellent sensitivity in the laboratory but relies on plasmonic structures that lack robustness and reproducibility suitable for analytical applications.

The question arises whether the same optical phenomena responsible for enhancement of the silicon Raman line in silicon nanopillars, nanowires, and nanocones[49−51] can be utilized to implement this concept and enhance Raman scattering of a thin sample layer on the surface of such silicon nanostructures.

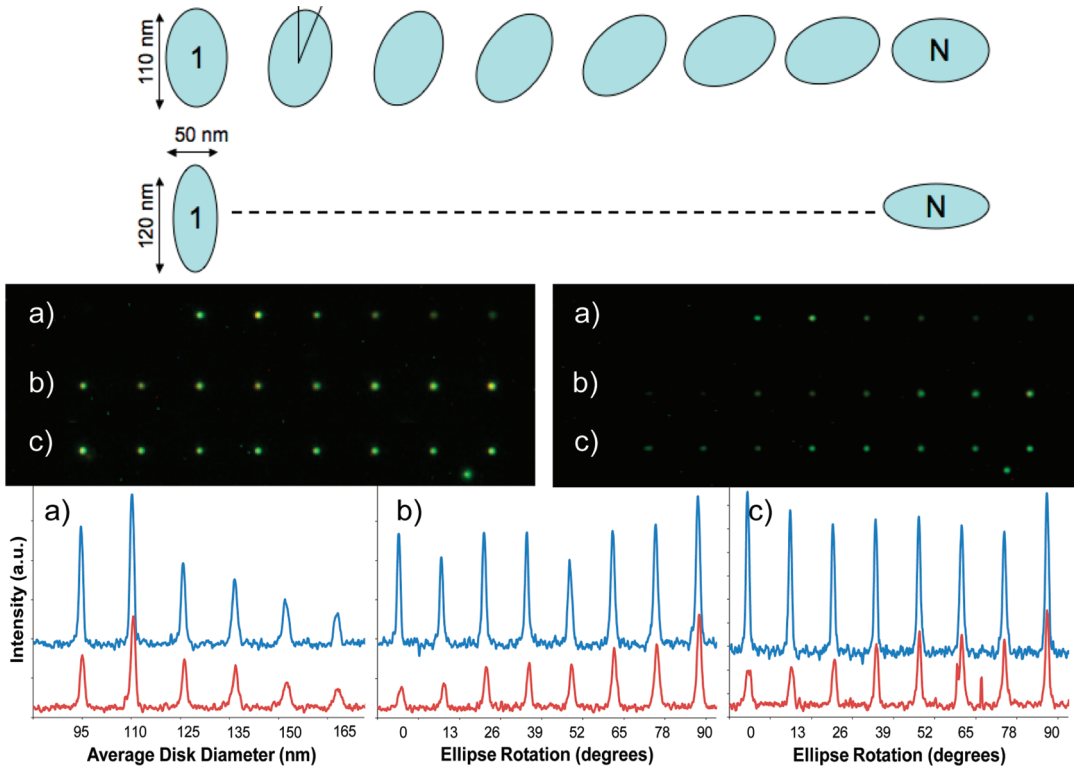


**Figure 6. Fluorescence images of FITC-coated type #5 nanopillars and two sets of elliptical nanopillars etched using the same RIE recipe. Fluorescence intensities in nonpolarized (left image) and polarized (right image) light are shown for (a) type #5 circular pillars with average pillar diameters in the range of 95−165 nm, (b) 110:70 nm elliptical pillars with the incrementally rotated major axis, and (c) 120:50 nm elliptical pillars with the incrementally rotated major axis. The intensity profiles for nonpolarized (top blue) and polarized (bottom red) light are shown in the respective a−c panels at the bottom.**

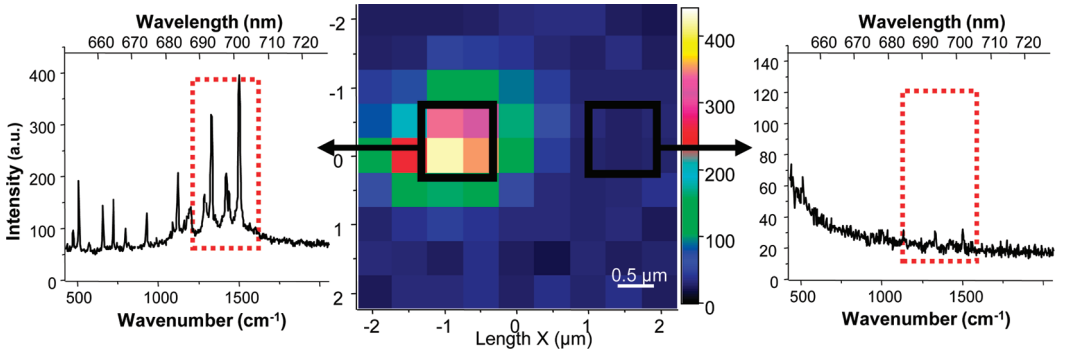


**Figure 7. Raster experiment is shown at center for the type #7 Si pillar (see SEM in Figure 1c and Table 1 data) with ~12 nm of ZcPc deposited at 45°, sample rotated 180°, then a second deposition of ~12 nm. Significant bands are highlighted in the Raman spectra for the off-pillar case on the right and the on-pillar case on the left. The ratios of the areas of the on-to-off-pillar 1500 $cm^{-1}$ bands for polarizations that are parallel (shown here) and perpendicular (not shown) to the source substrate line-of-sight are, respectively, 19.3 and 4.4.**

In order to address this question, a thin layer of zinc phthalocyanine (ZnPc) was vapor deposited onto chips with nanopillars (type #7) and used as a model analyte with relatively strong Raman scattering. As a result of two deposition steps (see details in Materials and Methods), approximately 24 nm of ZnPc was deposited on the silicon wafer surrounding the pillars while the thickness of the ZnPc layer on the pillar sidewalls had a crescent distribution with estimated maximum and average values of, respectively, 12 and 8 nm. This geometry corresponds to <30 attomoles of ZnPc present on the nanopillar surface.

Figure 7 shows a Raman map of the area around a single pillar. Acquisition time of 10 s was used for each point. The left side of Figure 7 shows the Raman spectrum of ZnPc when the probing beam was focused on the nanopillar, while the spectrum on the right shows the off-pillar signal. When the polarization of the probing beam was parallel to the line connecting parts of the nanopillar sidewalls with thickest ZnPc deposits,

the on-pillar to off-pillar Raman signal ratio was approximately 20. When the polarization was perpendicular to the deposition direction, the signal ratio was only about 5. The different ratios are consistent with the directional nature of the vapor deposition process and presence of crescent-shaped ZnPc deposits on the nanopillar sidewalls.

**Enhancement Factor Determination.** A nanopillar, area-corrected enhancement factor from the nanopillar structure was determined to assess the analytical utility of this system when scaled up. As such, EFs were determined for three representative cases: (1) Raman (phonon line of the single-crystal Si), (2) SERS (ZnPc), and (3) SEF (NHS-rhodamine). Initially, the average enhancement for the entire pillar structure (type #5) was looked at based on the results from the first silicon Raman line nanopillar trials. Using eq 1 seen in the Materials and Methods section, which compares the raw signal increase (RSI) based on the background-corrected on *versus* off nanopillar signal ratio, and the fractional change in analyte amount due to the nanopillar ($\Delta An$), the overall EF for the pillar is calculated. Average pillar diameter was used in determining $\Delta An$. The Materials and Methods section provides example calculations. The RSI for the type #5 pillar was found to be 7.04 (see Table 1), while the $\Delta An$ is based on the assumption that the analyte (silicon material) that is optically probed is approximately 100 nm thick. For this particular pillar set, the EF was found to be ~510. This is a strong enhancement and comparable with that obtained by others.[19]

The next set of calculations was based on the nanopillar being an appropriate structure to perform enhanced Raman analysis of a sample layer, in analogy to thin films on SERS-active substrates. The known amount of ZnPc deposited onto the surface of the pillar (type #7) made a strong test case. Equation 1 was used again, and this time the RSI was found to be 18 at the 1500 $cm^{-1}$ Raman band (Figure 7), while the $\Delta An$ is based on the ZnPc thickness on the pillar as well as on the silicon wafer floor. The EF for the type #7 pillar, with respect to ZnPc, is found to be ~200. While this is a modest level of enhancement when compared to plasmonic SERS-active structures, it is the first convincing demonstration of acquiring a SERS signal of a sample material using the light-focusing properties of silicon nanopillars without metal. Furthermore, the enhancement reported is averaged over the entire nanopillar structure; EF can be significantly greater when defined specifically for a very small fraction of the nanopillar surface where local field reaches maximum values.

Finally, even though calculating enhancement for SEF is usually conducted as a comparison between signal on and off of the structure, an alternative calculation similar to that of SERS enhancement can also be made with eq 1. For this calculation, the type #5 pillar system with NHS-rhodamine was considered. The RSI was found to be approximately 35 as discussed earlier (Figure 5). The $\Delta An$ was determined with the assumption that the APTES was coated in an ultrathin layer, basing the calculations on areas for the on-pillar and off-pillar cases. The EF was found to be ~120.

## CONCLUSIONS

Using FDTD numerical analysis, we predicted approximately 2 orders of magnitude enhancements of the local field intensity in the vicinity of appropriately designed and coaxially illuminated individual silicon nanopillars. Although optimized plasmonic systems that exhibit LSPR are capable of enhancing local fields to a significantly higher degree, the main advantage of the silicon nanopillar resonators is that they enhance fields in substantially larger volumes. We implemented such a nanopillar structure using a deterministic, wafer level nanofabrication sequence and for the first time experimentally measured enhanced Raman and fluorescence signals generated in this system in the presence of several different model sample materials. The magnitudes of the measured enhanced Raman and SEF signals as well the dependencies of these signals on the nanopillar geometry are generally consistent with our theoretical predictions. Analysis of our experimental data indicates that silicon nanopillar structures can provide fluorescence enhancements comparable or even stronger than those typically achieved using plasmonic SEF structures. We believe that nonplasmonic SERS with moderate EF will be instrumental when chemically specific detection is critical while samples are available in relatively large amounts. These amounts can be still remarkably small compared to limits of detection of other methods: in our preliminary experiments, excellent Raman signal was generated from <30 attomoles of ZnPc.

It is anticipated that properly designed massive arrays of silicon nanopillars will enable SEF assays with extremely high sensitivity while also addressing problems, such as oxidation and sulfur poisoning, present in plasmon-based SEF systems. Further improvements in analytical figures of merit, in particular, defined as the lowest surface concentration that yields Raman or fluorescence signal above the noise floor, are expected by extending our approach to silicon nanopillars arranged into dense arrays. Interaction between nanopillars in arrays can to some degree homogenize the field, which can be bad or good depending on the application. A recent study by Sturmberg *et al.*[20] points to a nontrivial task of optimizing silicon nanopillar arrays for enhanced optical absorption. Even more complex behavior can be anticipated when optimization of silicon nanopillar arrays aims at maximizing local field enhancement. Therefore, further

theoretical analysis and experiments are needed in order to gain more comprehensive understanding of the fundamental mechanisms responsible for the observed behaviors.

## MATERIALS AND METHODS

**Silicon Nanopillar Fabrication.** We used a fabrication sequence that relied on EBL, metal mask lift-off patterning, and anisotropic RIE of silicon as described previously.[52] Detailed steps of this sequence are as follows. A 300 nm film of ZEP 520A, a high-resolution positive tone resist suspended in anisole, was applied to the wafer using spin coating at 6000 rpm for 45 s onto a 4 in. silicon ⟨100⟩ wafer. Once coated, the wafer was then baked at 180 °C for 2 min and placed under vacuum in the JEOL JBX-9300 FS/E EBL system (100 keV thermal field emission gun).

Individual features were exposed to a 420 $\mu$C/cm$^2$ dose for writing, yielding circles and ellipses with targeted diameters ranging from 50 to 150 nm. Each circle or ellipse had 5 $\mu$m of space between other features and was laid out in ascending diameter from left to right while duplicating each row for a total of six of each diameter (see Figure 5). Following beam exposure, the wafer was developed in xylene and then introduced to an $O_2$ plasma (Oxford reactive ion etcher).

In order to create a masking layer for the RIE of silicon, a 20 nm chromium layer was deposited onto the surface of the wafer using an electron-beam dual gun evaporation chamber (Thermonics Laboratory, VE-240). The excess resist and chromium were then removed *via* lift-off using an acetone bath followed by isopropyl alcohol and deionized water rinses. Anisotropic RIE of silicon was then performed using a combination of inductively coupled plasma (ICP) and capacitively coupled plasma (CCP) conditions. ICP power, CCP power, pressure, substrate temperature, and a chemical composition of the plasma were adjusted to achieve the targeted nanopillar with close to vertical sidewalls. Plasma composition was varied by changing flow rates of the three processing gases: argon, sulfur hexafluoride, and octafluorocyclobutane. Different nanopillar heights were obtained by varying etch times. To determine exact dimensions of each pillar with a given etch recipe, we used scanning electron microscope (SEM) images.

**FDTD Analysis.** FDTD Solutions software package (Lumerical Inc.) was used in our simulations of the fabricated structures in order investigate their optical behaviors, in particular, their ability to enhance the local field. In order to take into account effects of various components of our experimental system, we compiled a series of 3D FDTD models that were composed of an individual silicon nanopillar, a silicon substrate, and a Gaussian light source impinging on the pillar coaxially (Figure 2a). Perfectly matching layer (PML) boundary conditions with 36 layers were used on all sides. The sizes of the simulated volume were 10 $\mu$m × 10 $\mu$m × 4.5 $\mu$m ($X \times Y \times Z$), large enough to accommodate a converging Gaussian source without truncating the beam. The Gaussian beam source was set to have propagation direction opposite to the $Z$-axis (*i.e.*, top to bottom) and linear polarization parallel to the $X$-axis. The source parameters were selected to span the wavelength region of 475 to 675 nm. Throughout the simulated volume outside the nanopillar region, we used a variable mesh size with a maximum size of 50 nm × 50 nm × 20 nm ($X \times Y \times Z$). A refined mesh with a constant step of 5 nm × 5 nm × 2 nm ($X \times Y \times Z$) was used in the region that included the pillar plus at least 20 nm margins outside the nanopillar along each axis. The main variable parameters of our simulations included (i) pillar diameter, (ii) pillar height, and (iii) Gaussian beam convergence. The results of the performed simulations were analyzed by evaluating local field intensity in the following planes: (ii) perpendicular to the $Y$-axis at $X = 0$, (ii) perpendicular to the $X$-axis at $Y = 0$, perpendicular to the $Z$-axis at $Z = 200$ nm (for shorter pillars) and $Z = 800$ nm.

**Raman Spectroscopy and EF Calculations.** All Raman spectra were collected using a JY-Horiba LabRam microscope. Details of the instrument setup have been described previously.[52,53] A 50× (0.45 NA, ∞) microscope objective was used to deliver 0.67 mW of the 633 nm line of a thermoelectrically stabilized HeNe laser with a spot size of approximately 2.5 $\mu$m. All spectra were collected with a backscattering geometry. Sample acquisition times were generally set to 3 s. Silicon Raman signal was optimized by fine-focusing the microscope objective, and the maps of Raman spectroscopic signals were collected while rastering the laser beam across each pattern at 0.5 $\mu$m intervals (1 spectral acquisition per step) over a single pillar (see Figure 3). SERS spectra were manually corrected for the broad background scatter using the LabSpec 4.12 software of our Raman system.

Enhancement factors (EFs) were computed using eq 1:

$$\mathrm{EF} = \frac{\mathrm{RSI}}{\Delta An} \tag{1}$$

where RSI is the raw signal increase (*i.e.*, the ratio of the areas of the Si 500 cm$^{-1}$ band, Raman ZnPc 1500 cm$^{-1}$ band, or the fluorescence NHS-rhodamine signal) on-pillar (corrected for off-pillar background) divided by the off-pillar background for the pillar under investigation. The RSI values can be found in Table 1 for the silicon Raman case, Figure 7 for ZnPc, and Figure 5 for NHS-rhodamine. $\Delta An$ is the fractional increase in analyte amount (computed as volume or area) due to the presence of the nanopillar (approximated as a cylinder for EF estimates). The fractional increase can be generally calculated using the equation

$$\Delta An = \frac{\pi D h t_1}{\pi W^2 t_2} \tag{2}$$

where the parameters are diameter ($D$) and height ($h$) of the pillar and the focused laser beam of spot size waist ($W = 1250$ nm). Also, $t$ is the analyte thickness on the pillar ($t_1$) and Si floor ($t_2$). Tor determine volumes, the depth of the analyte material was taken as the thickness of the vapor-deposited ZnPc film or estimated to be 100 nm when considering the Si base material. In the case of the fluorescence of NHS-rhodamine, an ultrathin layer was assumed to be due to the APTES linker and, thus, areas (rather than volumes) were used. In this case, a pixel of the microscope area detector (1 $\mu$m$^2$) and the nanopillar surface area were used. The calculated EF in each case is then reported as the average for the entire nanopillar structure; localized values can be significantly higher. Calculation details for the cases discussed in the Results and Discussion section appear below.

Case 1 Si Raman: type #5 silicon pillar with 100 nm analyte (Si base material) thickness:

$$\mathrm{RSI} = 7.0 \quad \Delta An = \pi(47\ \mathrm{nm})^2\ 975\ \mathrm{nm}/\pi(1250\ \mathrm{nm})^2$$
$$100\ \mathrm{nm} = 0.0138\ \mathrm{EF} = 7.0/0.0138 = \sim 510$$

Case 2 ZnPc SERS: type #7 silicon pillar with $t_1 = 8$ nm (based on 12 nm of ZnPc on each side of the pillar and shadowing effects) and $t_2$ is 24 nm:

$$\mathrm{RSI} = 18 \quad \Delta An = \pi 180\ \mathrm{nm}\ 2300\ \mathrm{nm}\ 8\mathrm{nm}/\pi(1250\ \mathrm{nm})^2$$
$$24\ \mathrm{nm} = 0.088\ \mathrm{EF} = 19/0.88 = \sim 200$$

Case 3 SEF: type #5 silicon pillar , APTES-rhodamine ultrathin layer:

$$\mathrm{RSI} = 35 \quad \Delta An = \text{nanopillar area/pixel area}$$
$$= 2.91 \times 10^5\ \mathrm{nm}^2/1.0 \times 10^6\ \mathrm{nm}^2 = 0.291\ \mathrm{EF}$$
$$= 35/0.291 = \sim 120$$

**Microscopy.** Scanning electron microscope (SEM) images were collected with an FEI dual beam SEM/FIB microscope with a field emission gun operating at approximately 5.00 kV, altered slightly depending on the angle of imaging. Sample damage and charge buildup were reduced under these conditions, yielding moderate-resolution images of the Si pillar substrates.

All optical microscopic images were obtained using a Nikon Eclipse 100 microscope using a 100× microscope objective. The microscope was equipped with a high-pressure broad-band Hg light source, a multicolor fluorescence cube (DAPI-FITC-TRITC),[54] and a Digital Sight CCD camera (DS-2M, Nikon, Inc.) controlled by NIS-Elements software.

**Substrate Preparation.** After fabrication, some pillars were fluorescently labeled for imaging. Using a method described previously,[55] each piece of silicon wafer containing nanopillars was placed in a vial with anhydrous toluene with the addition of 3-aminopropyltriethoxysilane (APTES) to create a 10% solution by volume. The chips soaked in the APTES solution for 1 h at room temperature before being rinsed sequentially with toluene, methanol, and 18 MΩ deionized water (Barnstead, E-Pure). This process has been shown to yield a smooth, thin, uniform layer of APTES. From that point, one of two fluorescent dyes was used. Thirty microliters of a 1 mM solution of either NHS-rhodamine dye or FITC dye was spotted onto the pillars and allowed to bond to the chip (15 min for NHS-rhodamine and 45 min for FITC) before excess dye was removed.

Some of the fabricated nanopillars were coated with a thin layer of ZnPc. ZnPc was thermally evaporated onto the silicon chips with the pillars in a Cooke CVE 301 physical vapor deposition (PVD) system. In order to deposit comparable amounts of ZnPc on the nanopillar sidewalls and surrounding silicon substrate, the chips were mounted at a 45° angle with respect to the line of sight between the substrate and the evaporation source. After 12 nm of ZnPc was deposited, the substrate was rotated 180° and another 12 nm was deposited. The nominal thickness of the deposited ZnPc was monitored with a QCM mounted in the PVD. As a result of this procedure, approximately 24 nm of ZnPc was deposited on the silicon wafer surrounding the pillars while the thickness of the ZnPc layer on the pillar sidewalls had a crescent distribution with estimated maximum and average values of, respectively, 12 and 8 nm.

*Conflict of Interest:* The authors declare no competing financial interest.

*Acknowledgment.* A portion of this research was conducted at the Center for Nanophase Materials Sciences, which is sponsored at Oak Ridge National Laboratory by the Scientific User Facilities Division, Office of Basic Energy Sciences, U.S. Department of Energy. N.V.L., I.I.K., and I.A.M. would like to acknowledge support from Office of Basic Energy Sciences, U.S. Department of Energy. M.J.S. would like to acknowledge contributing grants to the University of Tennessee from the U.S. Environmental Protection Agency STAR program and the U.S. Department of Energy, National Transportation Research Center.

## REFERENCES AND NOTES

1. Garnett, E. C.; Brongersma, M. L.; Cui, Y.; McGehee, M. D. Nanowire Solar Cells. *Annu. Rev. Mater. Sci.* **2011**, *41*, 269–295.
2. Fan, Z. Y.; Kapadia, R.; Leu, P. W.; Zhang, X. B.; Chueh, Y. L.; Takei, K.; Yu, K.; Jamshidi, A.; Rathore, A. A.; Ruebusch, D. J.; *et al.* Ordered Arrays of Dual-Diameter Nanopillars for Maximized Optical Absorption. *Nano Lett.* **2010**, *10*, 3823–3827.
3. Cao, L. Y.; Fan, P. Y.; Vasudev, A. P.; White, J. S.; Yu, Z. F.; Cai, W. S.; Schuller, J. A.; Fan, S. H.; Brongersma, M. L. Semiconductor Nanowire Optical Antenna Solar Absorbers. *Nano Lett.* **2010**, *10*, 439–445.
4. Sivakov, V.; Andrae, G.; Gawlik, A.; Berger, A.; Plentz, J.; Falk, F.; Christiansen, S. H. Silicon Nanowire-Based Solar Cells on Glass: Synthesis, Optical Properties, and Cell Parameters. *Nano Lett.* **2009**, *9*, 1549–1554.
5. Cao, L. Y.; White, J. S.; Park, J. S.; Schuller, J. A.; Clemens, B. M.; Brongersma, M. L. Engineering Light Absorption in Semiconductor Nanowire Devices. *Nat. Mater.* **2009**, *8*, 643–647.
6. Tian, B.; Zheng, X.; Kempa, T. J.; Fang, Y.; Yu, N.; Yu, G.; Huang, J.; Lieber, C. M. Coaxial Silicon Nanowires as Solar Cells and Nanoelectronic Power Sources. *Nature* **2007**, *449*, 885-U8.
7. Servati, P.; Colli, A.; Hofmann, S.; Fu, Y. Q.; Beecher, P.; Durrani, Z. A. K.; Ferrari, A. C.; Flewitt, A. J.; Robertson, J.; Milne, W. I. Scalable Silicon Nanowire Photodetectors. *Physica E* **2007**, *38*, 64–66.
8. Yang, C.; Barrelet, C. J.; Capasso, F.; Lieber, C. M. Single P-Type/Intrinsic/N-Type Silicon Nanowires as Nanoscale Avalanche Photodetectors. *Nano Lett.* **2006**, *6*, 2929–2934.
9. Canham, L. T. Silicon Quantum Wire Array Fabrication by Electrochemical and Chemical Dissolution of Wafers. *Appl. Phys. Lett.* **1990**, *57*, 1046–1048.
10. Hu, J. T.; Odom, T. W.; Lieber, C. M. Chemistry and Physics in One Dimension: Synthesis and Properties of Nanowires and Nanotubes. *Acc. Chem. Res.* **1999**, *32*, 435–445.
11. Hafaiedh, A.; Bouarissa, N. Quantum Confinement Effects on Energy Gaps and Electron and Hole Effective Masses of Quantum Well AlN. *Physica E* **2011**, *43*, 1638–1641.
12. Yan, R.; Gargas, D.; Yang, P. Nanowire Photonics. *Nat. Photonics* **2009**, *3*, 569–576.
13. Bronstrup, G.; Jahr, N.; Leiterer, C.; Csaki, A.; Fritzsche, W.; Christiansen, S. Optical Properties of Individual Silicon Nanowires for Photonic Devices. *ACS Nano* **2010**, *4*, 7113–7122.
14. Cao, L. Y.; Fan, P. Y.; Barnard, E. S.; Brown, A. M.; Brongersma, M. L. Tuning the Color of Silicon Nanostructures. *Nano Lett.* **2010**, *10*, 2649–2654.
15. Walker, B. N.; Stolee, J. A.; Pickel, D. L.; Retterer, S. T.; Vertes, A. Tailored Silicon Nanopost Arrays for Resonant Nanophotonic Ion Production. *J. Phys. Chem. C* **2010**, *114*, 4835–4840.
16. Seo, K.; Wober, M.; Steinvurzel, P.; Schonbrun, E.; Dan, Y.; Ellenbogen, T.; Crozier, K. B. Multicolored Vertical Silicon Nanowires. *Nano Lett.* **2011**, *11*, 1851–1856.
17. Cao, L. Y.; Park, J. S.; Fan, P. Y.; Clemens, B.; Brongersma, M. L. Resonant Germanium Nanoantenna Photodetectors. *Nano Lett.* **2010**, *10*, 1229–1233.
18. Muskens, O. L.; Diedenhofen, S. L.; Kaas, B. C.; Algra, R. E.; Bakkers, E.; Rivas, J. G.; Lagendijk, A. Large Photonic Strength of Highly Tunable Resonant Nanowire Materials. *Nano Lett.* **2009**, *9*, 930–934.
19. Cao, L. Y.; Nabet, B.; Spanier, J. E. Enhanced Raman Scattering from Individual Semiconductor Nanocones and Nanowires. *Phys. Rev. Lett.* **2006**, *96*, 157402.
20. Sturmberg, B. C. P.; Dossou, K. B.; Botten, L. C.; Asatryan, A. A.; Poulton, C. G.; de Sterke, C. M.; McPhedran, R. C. Modal Analysis of Enhanced Absorption in Silicon Nanowire Arrays. *Opt. Express* **2011**, *19*, A1067–A1081.
21. Schmidt, V.; Senz, S.; Gosele, U. Diameter-Dependent Growth Direction of Epitaxial Silicon Nanowires. *Nano Lett.* **2005**, *5*, 931–935.
22. Taraci, J. L.; Dailey, J. W.; Clement, T.; Smith, D. J.; Drucker, J.; Picraux, S. T. Nanopillar Growth Mode by Vapor–Liquid–Solid Epitaxy. *Appl. Phys. Lett.* **2004**, *84*, 5302–5304.
23. Ergen, O.; Ruebusch, D. J.; Fang, H.; Rathore, A. A.; Kapadia, R.; Fan, Z.; Takei, K.; Jamshidi, A.; Wu, M.; Javey, A. Shape-Controlled Synthesis of Single-Crystalline Nanopillar Arrays by Template-Assisted Vapor–Liquid–Solid Process. *J. Am. Chem. Soc.* **2010**, *132*, 13972–13974.
24. Wells, S. M.; Polemi, A.; Lavrik, N. V.; Shuford, K. L.; Sepaniak, M. J. Efficient Disc on Pillar Substrates for Surface Enhanced Raman Spectroscopy. *Chem. Commun.* **2011**, *47*, 3814–3816.
25. De Jesus, M. A.; Giesfeldt, K. S.; Oran, J. M.; Abu-Hatab, N. A.; Lavrik, N. V.; Sepaniak, M. J. Nanofabrication of Densely Packed Metal-Polymer Arrays for Surface-Enhanced Raman Spectrometry. *Appl. Spectrosc.* **2005**, *59*, 1501–1508.
26. Polemi, A.; Wells, S. M.; Lavrik, N. V.; Sepaniak, M. J.; Shuford, K. L. Local Field Enhancement of Pillar Nanosurfaces for SERS. *J. Phys. Chem. C* **2010**, *114*, 18096–18102.
27. Blech, M. D.; Eibert, T. F. A Dipole Excited Ultrawideband Dielectric Rod Antenna with Reflector. *IEEE Trans. Antennas Propag.* **2007**, *55*, 1948–1954.
28. Ausman, L. K.; Schatz, G. C. On the Importance of Incorporating Dipole Reradiation in the Modeling of Surface Enhanced Raman Scattering from Spheres. *J. Chem. Phys.* **2009**, *131*, 084708.
29. Ausman, L. K.; Schatz, G. C. Whispering-Gallery Mode Resonators: Surface Enhanced Raman Scattering Without Plasmons. *J. Chem. Phys.* **2008**, *129*, 054704.

30. Luu, Q. N.; Doorn, J. M.; Berry, M. T.; Jiang, C. Y.; Lin, C. K.; May, P. S. Preparation and Optical Properties of Silver Nanowires and Silver-Nanowire Thin Films. *J. Colloid Interface Sci.* **2011**, *356*, 151–158.
31. Shtoyko, T.; Matveeva, E. G.; Chang, I. F.; Gryczynski, Z.; Goldys, E.; Gryczynski, I. Enhanced Fluorescent Immunoassays on Silver Fractal-like Structures. *Anal. Chem.* **2008**, *80*, 1962–1966.
32. Hossain, M. K.; Huang, G. G.; Kaneko, T.; Ozaki, Y. Characteristics of Surface-Enhanced Raman Scattering and Surface-Enhanced Fluorescence Using a Single and a Double Layer Gold Nanostructure. *Phys. Chem. Chem. Phys.* **2009**, *11*, 7484–7490.
33. Medintz, I. L.; Uyeda, H. T.; Goldman, E. R.; Mattoussi, H. Quantum Dot Bioconjugates for Imaging, Labelling and Sensing. *Nat. Mater.* **2005**, *4*, 435–446.
34. Howarth, M.; Liu, W.; Puthenveetil, S.; Zheng, Y.; Marshall, L. F.; Schmidt, M. M.; Wittrup, K. D.; Bawendi, M. G.; Ting, A. Y. Monovalent, Reduced-Size Quantum Dots for Imaging Receptors on Living Cells. *Nat. Methods* **2008**, *5*, 397–399.
35. Xie, C.; Hanson, L.; Cui, Y.; Cui, B. Vertical Nanopillars for Highly Localized Fluorescence Imaging. *Proc. Natl. Acad. Sci. U.S.A.* **2011**, *108*, 3894–3899.
36. Aslan, K.; Gryczynski, I.; Malicka, J.; Matveeva, E.; Lakowicz, J. R.; Geddes, C. D. Metal-Enhanced Fluorescence: An Emerging Tool in Biotechnology. *Curr. Opin. Biotechnol.* **2005**, *16*, 55–62.
37. Pieczonka, N. P. W.; Goulet, P. J. G.; Aroca, R. F. *Applications of the Enhancement of Resonance Raman Scattering and Fluorescence by Strongly Coupled Metallic Nanostructures*; Springer: Berlin, Germany, 2006; Vol. 103.
38. Larmour, I. A.; Graham, D. Surface Enhanced Optical Spectroscopies for Bioanalysis. *Analyst* **2011**, *136*, 3831–3853.
39. Lavrik, N. V.; Taylor, L. T.; Sepaniak, M. J. Nanotechnology and Chip Level Systems for Pressure Driven Liquid Chromatography and Emerging Analytical Separation Techniques: A Review. *Anal. Chim. Acta* **2011**, *694*, 6–20.
40. Lakowicz, J. R.; Geddes, C. D.; Gryczynski, I.; Malicka, J.; Gryczynski, Z.; Aslan, K.; Lukomska, J.; Matveeva, E.; Zhang, J. A.; Badugu, R.; *et al.* Advances in Surface-Enhanced Fluorescence. *J. Fluoresc.* **2004**, *14*, 425–441.
41. Corrigan, T. D.; Guo, S.; Phaneuf, R. J.; Szmacinski, H. Enhanced Fluorescence from Periodic Arrays of Silver Nanoparticles. *J. Fluoresc.* **2005**, *15*, 777–784.
42. Geddes, C. D.; Parfenov, A.; Roll, D.; Fang, J. Y.; Lakowicz, J. R. Electrochemical and Laser Deposition of Silver for Use in Metal-Enhanced Fluorescence. *Langmuir* **2003**, *19*, 6236–6241.
43. Geddes, C. D.; Parfenov, A.; Roll, D.; Gryezynski, I.; Malicka, J.; Lakowicz, J. R. Roughened Silver Electrodes for Use in Metal-Enhanced Fluorescence. *Spectrochim. Acta A* **2004**, *60*, 1977–1983.
44. Matveeva, E.; Gryczynski, Z.; Malicka, J.; Gryczynski, I.; Lakowicz, J. R. Metal-Enhanced Fluorescence Immunoassays Using Total Internal Reflection and Silver Island-Coated Surfaces. *Anal. Biochem.* **2004**, *334*, 303–311.
45. Fort, E.; Gresillon, S. Surface Enhanced Fluorescence. *J. Phys. D: Appl. Phys.* **2008**, *41*, 013001.
46. Anger, P.; Bharadwaj, P.; Novonty, L. Enhancement and Quenching of Single-Molecule Fluorescence. *Phys. Rev. Lett.* **2006**, *96*, 113002.
47. Moskovits, M. Surface-Enhanced Spectroscopy. *Rev. Mod. Phys.* **1985**, *57*, 783–826.
48. Schatz, G.; Young, M. A.; Van Duyne, R. P. *Electromagnetic Mechanism of SERS*; Springer: Berlin, Germany, 2006; Vol. 103.
49. Claps, R.; Dimitropoulos, D.; Han, Y.; Jalali, B. Observation of Raman Emission in Silicon Waveguides at 1.54 $\mu$m. *Opt. Express* **2002**, *10*, 1305–1313.
50. Boyraz, O.; Jalali, B. Demonstration of a Silicon Raman Laser. *Opt. Express* **2004**, *12*, 5269–5273.
51. Rong, H. S.; Jones, R.; Liu, A. S.; Cohen, O.; Hak, D.; Fang, A.; Paniccia, M. A Continuous-Wave Raman Silicon Laser. *Nature* **2005**, *433*, 725–728.
52. Wells, S. M.; Retterer, S. D.; Oran, J. M.; Sepaniak, M. J. Controllable Nanotabrication of Aggregate-like Nanoparticle Substrates and Evaluation for Surface-Enhanced Raman Spectroscopy. *ACS Nano* **2009**, *3*, 3845–3853.
53. De Jesus, M. A.; Giesfeldt, K. S.; Sepaniak, M. J. Use of a Sample Translation Technique to Minimize Adverse Effects of Laser Irradiation in Surface-Enhanced Raman Spectrometry. *Appl. Spectrosc.* **2003**, *57*, 428–438.
54. Scordata, A.; Schwartz, S. Triple Band Excitation: EAPI-FITC-TRITC. *Fluorescence Filter Combinations*; Nikon Instruments, Inc.: New York, 2010; Vol. 2011.
55. Howarter, J. A.; Youngblood, J. P. Optimization of Silica Silanization by 3-Aminopropyltriethoxysilane. *Langmuir* **2006**, *22*, 11142–11147.